Limitations of the multichannel analysis of surface waves (MASW) method for subsurface anomaly detection

J. A. Crocker
The University of Texas at Austin, Austin, USA, jcrocker@utexas.edu

J. P. Vantassel[1], U. Arslan[2], B. R. Cox[3]
The University of Texas at Austin, Austin, USA, jvantassel@utexas.edu[1], uarslan@utexas.edu[2], brcox@utexas.edu[3]

ABSTRACT: This study assesses the practical limitations of using the multichannel analysis of surface waves (MASW) method for detecting subsurface anomalies. The sensitivity of MASW dispersion data to the presence of subsurface anomalies is examined through various two-dimensional (plane-strain) finite-difference elastic wave-propagation simulations. These simulations were performed on models with anomalies of varying size, stiffness, and depth. The misfit between the dispersion data from a model with an anomaly (treatment model) and the same model without an anomaly (control model) were compared as a quantitative means of discerning if the anomaly was reliably detectable (i.e., outside the bounds of common dispersion data uncertainty). The ability of MASW to detect an anomaly of a given size, stiffness, and depth is summarized in normalized figures, which are intended as a feasability tool for those seeking to use MASW for anomaly detection.

Keywords: surface waves; site characterization; multichannel analysis of surface waves; anomaly detection

1. Introduction

In order to perform geotechnical design, it is necessary to obtain accurate information regarding the characteristics of the subsurface, which include the subsurface material's physical properties and spatial variability. Unfortunately, obtaining extensive information with the current state-of-practice remains highly impractical. This is especially true when using invasive methods, such as drilling boreholes, due to the time and cost involved. As a result of the need for more complete information in recent years, non-invasive methods, especially those capable of producing two- and three-dimensional subsurface images, have seen a marked increase in their popularity. These methods include refraction tomography, reflection tomography, electrical resistivity imaging (ERI), full-waveform inversion (FWI), and the multichannel analysis of surface waves (MASW) method [1-4]. This study will focus on the MASW method due to its wide-spread use.

The MASW method [5] was developed as a relatively inexpensive and efficient non-invasive test which uses the propagation of surface waves to evaluate subsurface stiffness. MASW involves recording actively generated surface waves as they travel down a linear array of receivers. These recordings are then processed to obtain surface wave dispersion data using one of several two-dimensional (i.e., time and space) transformations [6, 7]. This estimate of the site's surface wave dispersion characteristics (i.e., the variation of surface wave velocity as a function of frequency or wavelength) is often referred to as the experimental dispersion curve. This measurement of the site's dispersion is generally not the end goal, but rather is inverted to produce an estimate of the site's one-dimensional shear-wave velocity (V_s) profile. This profile is generally believed to be representative of the soil beneath the center of the array [8]. Multiple 1D V_s profiles may then be combined and interpolated to form a pseudo-2D image of the subsurface.

This process for using MASW to develop a pseudo-2D subsurface image has shown varying degrees of success in literature, particularly regarding the detection of subsurface irregularities. For example, when comparing the MASW method to seismic refraction and ERI, Groves et al. [9] found that MASW testing was the most successful at detecting three distinct soil layers at the near-surface (i.e., the top 4 m) and that it was able to detect an increase in stiffness due to a large till layer located approximately 4.6 to 10.7 m deep across the site, but provided an inaccurate estimate of the depth to that layer. In contrast, ERI was shown to provide the most accurate estimate to the soil-till interface. Alternatively, Ismail et al. [10] found that the MASW method was not able to provide high vertical or lateral resolution of soil layers compared to the shear-wave reflection method but provided relatively better V_s measurements at a lower time and cost. Mahvelati and Coe [11] found that using MASW testing to detect the geometry of unknown bridge foundations could produce mixed results. Specifically, the lateral extent of the bridge's foundation was relatively accurate while the depth and thickness were smaller than expected based on prior knowledge regarding the foundation's design. Nolan et al. [12] used a shallow, man-made void to illustrate the accuracy of MASW testing. They found that it was possible to detect a subsurface anomaly using MASW, although there was limited resolution in both the vertical and lateral geometry of the void. Pan et al. [13] analyzed the ability of MASW testing to detect lateral heterogeneity by creating a synthetic model containing a checkerboard pattern of stiff and soft soil. They discovered that MASW had poor resolution and the checkerboard model could not be recovered, whereas using the same model analyzed with FWI allowed for much higher resolution.

Given the mixed conclusions regarding the MASW method's ability to detect and accurately resolve underground irregularities, this paper seeks to evaluate the possibility of detecting subsurface anomalies by using a variety of synthetic models and the MASW method. In this study, MASW-style testing is performed numerically on a control model without an anomaly and a number of treatment models containing anomalies of varying size, location, and stiffness. Each model contains a simulated array of receivers and multiple source locations based on testing parameters commonly found in literature. As a simplification each anomaly was rectangular in shape, homogenous, and centered underneath the array. The 2D finite-difference code DENISE was used to simulate the MASW wavefield [14]. The experimental waveforms were then processed using standard MASW techniques to estimate an experimental dispersion curve. The misfit between the experimental dispersion curves from each treatment and control model pair was then calculated. The misfit values were then summarized in figures for use as a guide to quantify the feasibility of detecting a subsurface anomaly.

2. Methodology

2.1. MASW method

The MASW method relies upon the propagation of surface waves (Rayleigh or Love) to evaluate subsurface soil stiffness. The velocity (v) of the waves as they travel through the subsurface is dependent not only on the properties of the material through which they propagate, but also on their frequency (f). This dependence of the waves' phase velocities on frequency is called dispersion. The dispersive nature of surface waves is useful for site characterization because the depth of penetration into the ground may be thought of as a function of a wave's measured wavelength ($\lambda = v/f$). A rough estimate of the depth to which the wave can "see" (i.e., d_{max}) is generally approximated to be about half its wavelength ($\lambda/2$). Therefore, given that frequency and wavelength have an inverse relationship, it follows that a low f corresponds to a longer λ and vice versa. Consequently, higher frequencies will propagate at velocities corresponding to shallower layers, while lower frequencies will propagate at velocities that are influenced by both the shallow and deeper layers, as illustrated schematically in Fig. 1.

To perform MASW testing, a seismic source is operated in-line with the axis of the array of receivers to generate surface waves, which are then recorded by the array of receivers. The array of receivers can vary in number (generally between 12 and 96) and spacing (generally between 0.5 and 5 m). Because it is believed the length of the receiver array governs the data's horizontal resolution, care should be taken when determining appropriate parameters to use while testing [16]. Furthermore, the length of the array should also be chosen based on the desired depth of investigation. It is typical to choose an array length that is at least twice the investigation depth, or equal to the maximum desired wavelength [17]. Additionally, a seismic source with appropriate frequency bandwidth should be chosen based on desired testing depths due to the relationship between depth of penetration and the surface wave frequency. Multiple shot offsets (i.e., the distance from the source to the nearest receiver in the array) may be used to improve gathered data [17]. It is also important to choose proper shot offsets for the mitigation of near-field effects.

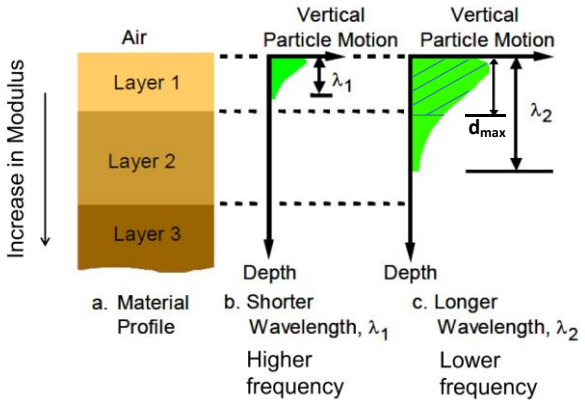

Figure 1. The relationship between surface wave vertical particle motion, wavelength, and frequency are shown. Note that shorter wavelengths correspond to higher frequencies, whereas longer wavelengths correspond to lower frequencies. Fig. 1b shows one wavelength, while Fig. 1c shows d_{max}, or $\lambda/2$, which is the "visible" depth [modified from 15].

The recorded time histories gathered by the array can then be analyzed to obtain measurements of the site's dispersion characteristics. This is completed by using any number of various two-dimension wavefield transformations, with the simplest being a two-dimensional Fourier transform to the frequency-wavenumber (i.e., f-k) domain [6]. The points of maximum power of this two-dimensional transformation represent a measurement of the surface waves' dispersion, and these measurements are typically represented by plotting phase velocity as a function of frequency. Ultimately, these measurements of phase velocity are inverted to obtain a 1D V_s profile. If multiple MASW arrays were set up in close proximity to one another, their resulting 1D V_s profiles can be contoured to produce a pseudo-2D and, in certain cases, a pseudo-3D image. The purpose of this work is to primarily assess the first stage of this process (i.e., the ability to detect an anomaly at the dispersion stage). However, it should be noted that detecting an anomaly at the dispersion stage does not imply that it can be accurately resolved during the inversion phase. Accurately resolving the depth, size, and stiffness of an anomally via inversion is a much more complicted problem due to the non-unique nature of inverse problems.

2.2. Model development

To simulate MASW testing, DENISE, a 2D plane-strain finite-difference program, was used [14]. This program simulates wave propagation by solving the 2D wave equation for an elastic medium. Each model was 256 m in length and 64 m in depth and discretized into square 0.25 m elements. The order of the finite-difference operator was eight, and PML boundary conditions were applied to the bottom and side faces of each model. In particular, the width of the absorbing frame was 25 gridpoints, and the frequency within the PML was 10 Hz.

The damping velocity was set to 1,500 m/s, and the degree of the damping function was 2. The remaining inputs for each model included user-defined receiver spacing, array length, source type, and sampling parameters, which are detailed in Section 2.3.

Each control model (i.e., with no anomaly present) was generated to contain a uniform body of soil (i.e., a half-space) with a constant density (ρ), Poisson's ratio (ν), and V_s. Two control models were considered, where one had V_s equal to 150 m/s and the other 300 m/s, while ρ and ν were held constant at 2,000 kg/m^3 and 0.33, respectively.

Various anomalies were then placed into each half-space to create the treatment models. These anomalies were selected to be noticeably softer/stiffer than the surrounding material. Specifically, impedance contrasts, defined as the ratio of the anomaly V_s to the half-space V_s, of 1.5, 2.0, and 5.0 were used for models containing a stiff anomaly, whereas values of 0.20, 0.50, and 0.67 were used for soft anomalies. This means for a half-space V_s of 150 m/s, stiff anomalies had V_s equal to 225, 300, and 750 m/s, while soft anomalies were created with V_s equal to 30, 75, and 100 m/s. Similarly, for a half-space V_s of 300 m/s, stiff anomalies had V_s equal to 450, 600, and 1,500 m/s, while soft anomalies were created to have values of V_s equal to 60, 150, and 200 m/s.

Each anomaly was centered under the array to represent a single snapshot in space representative of a traditional 2D MASW survey. An anomaly directly under the center of the array should yield the best opportunity to accurately detect and resolve it. To examine the sensitivity of MASW to the width of an anomaly, various lateral extents between 1 and 36 m were used. To test the vertical resolution of MASW, anomalies were placed at top depths increasing from 2 to 20 m. Anomaly thicknesses of 1, 2, and 4 m were also considered to assess the detectibility of various irregularities that may be present in soil. Fig. 2 is a schematic of a typical treatment model with the previously mentioned variables listed for ease of understanding.

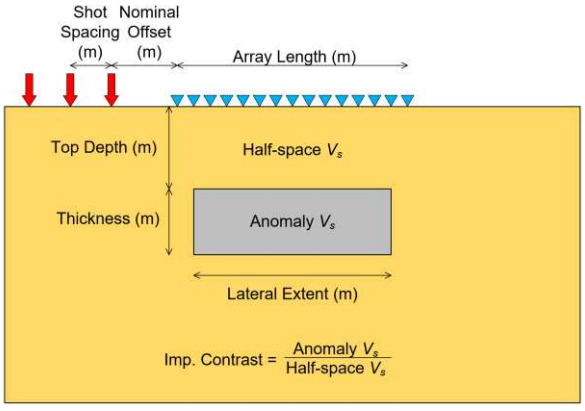

Figure 2. A general schematic for each treatment model is shown. The half-space and anomaly shear-wave velocities were varied to create a range of impedance contrasts, while the top depth, thickness, and lateral extent of each anomaly were varied to represent a set of possibilities that may be encountered during field testing. Roughly 300 models were created for each unique impedance contrast and half-space V_s pairing, such that over 3,000 models in total were created for all impedance contrasts.

Additionally, to more easily reference models, each model was assigned a unique identification code. Each code consists of a string of letters and numbers, which are representative of each variable and its value, as shown in Table 1. For example, given an anomaly that is 36 m wide, 4 m thick, at a depth of 20 m, and with an impedance contrast of 0.67 placed in a half-space with V_s equal to 150 m/s, the model may be identified as I0.67-H150-T4-D20-L36. Because over 3,000 unique models were generated for this study, this naming convention was adopted so that each model has a descriptive identifier that may be quickly referenced.

Table 1. Summary of model variables with associated values

Variable	Acronym	Values
Impedance Contrast	I	0.67, 0.2, 0.5; 1.5, 2.0, 5.0
Half-space V_s (m/s)	H	150, 300
Anomaly Thickness (m)	T	1, 2, 4
Top Depth (m)	D	2 – 20
Lateral Extent (m)	L	1, 4, 6, 10, 14, 19, 25, 30, 36

2.3. Model testing parameters

To ensure the 2D MASW testing was being performed in conformance with the standard of practice, a literature review was performed to summarize a "typical" test configuration. The literature review examined parameters such as array lengths, receiver spacings, and source frequency content. When analyzing various case studies, it was determined that 24 receivers spaced at approximately 1 m [4, 11, 18-20] were used to form an array. A minority of studies used 24 receivers with a receiver spacing greater than 1 m, though this was done explicitly in the hope of obtaining longer wavelengths and therefore deeper testing depths [3, 21-22]. Others chose to use a constant 1 m receiver spacing but utilized more than 24 receivers to similarly create longer array lengths [9, 12, 23]. Therefore, to be consistent with the majority of case histories, each simulation used 24 receivers spaced at 1 m for a total array length of 23 m.

In field tests, the cheapest and most commonly used seismic source is the sledgehammer. Sledgehammers weighing at least 5 kg can be used to obtain data across a relatively large frequency band, and many case studies have utilized sledgehammers with varying degrees of success [3-4, 11, 18-19, 21]. However, this source typically does not provide much energy at lower frequencies (less than 8 Hz), which means more powerful sources, such as an accelerated weight drop or vertically operated shaker, should be used if lower frequencies are desired [17]. Ultimately, it was decided that the simulations should be conducted under very favorable source conditions in order to provide the best chance at detecting anomalies, such that frequencies from 5 Hz – 100 Hz were considered for all models. Multiple sources were tested until data were obtained within this bandwidth, and it was determined that the desired source bandwidth was acquired using a fifth-order Butterworth filtered spike

wavelet. A timestep of 0.02 ms was used for a total record time of 3 s, and the output waveforms were then downsampled to 400 Hz.

After determining the array length and bandwidth of the seismic source, various shot locations were analyzed to determine which location(s) would provide the highest quality dispersion data. Near-field effects, which occur when surface waves have not yet fully developed before being recorded by a receiver, are caused by having a small offset between the array and the source. To avoid near-field effects, it is recommended that a source offset of at least three to five times the receiver spacing should be used [17]. In this study, an offset of ten times the receiver spacing, or -10 m, was used for the closest shot location. This was due to a shot location of -5 m yielding clear near-field data when compared to further offsets. It was determined that shot offsets of -10, -15, -20, and -25 m provided acceptable data without obvious near- or far-field effects for the majority of the models. Given that the models were known to be symmetric, shots were only required off one side of the array. A summary of testing parameters used in this study are included in Table 2.

Table 2. Summary of model testing parameters

No. of receivers	24
Receiver spacing	1 m
Array length	23 m
Type of source	Spike wavelet, 0-15 Hz
Sampling frequency	400 Hz
Record length	3 s
Nominal offset	-10 m
Source spacing	5 m

3. Data analysis

3.1. Processing dispersion data

After running the control and treatment models, the simulated waveforms were transformed in the frequency domain using the frequency domain beam former (FDBF) method [7]. The FDBF used an inverse-amplitude weighting scheme with a cylindrical steering vector. All calculations were performed over a frequency bandwidth of 1 – 200 Hz. After the transformation, the maximum spectral peak for each frequency was automatically chosen and plotted to form dispersion curves. The dispersion curves for multiple offsets were then plotted together and statistically combined to form a mean dispersion curve with uncertainty following the recommendations of [24]. Fig. 3a-b show examples of a dispersion image for a -10 m offset for models composed of a half-space with V_s equal to 300 m/s and an anomaly that is 2 m thick, 36 m wide, at a top depth of 5 m, and with a V_s of 60 m/s and 1,500 m/s (models I0.20-H300-T2-D5-L36 and I5.00-H300-T2-D5-L36), respectively. The hollow white circles identify the peak energy at each frequency. Fig. 3c-d show the combined dispersion data for all shot offsets for each model. It should be noted that the dispersion curves in Fig. 3c-d have not yet been processed to remove data points from higher modes, outliers, and data beyond the 5 Hz – 100 Hz frequency bandwidth.

Prior to binning dispersion data and calculating phase velocity statistics (mean and standard deviation), clear outliers were removed from each data set, as is standard for MASW. This was completed by visually determining which data significantly deviated from the mean of the dispersion data for a given frequency. Data below 5 Hz and above 100 Hz were omitted to provide a consistent, but optimistic, frequency bandwidth for all models. To ensure the dispersion data from all models were provided at the same frequencies, each set of dispersion data was logarithmically resampled between 5 and 100 Hz with 100 points.

When viewing the dispersion curves, higher mode trends were sometimes visible in addition to the fundamental mode. Although the fundamental mode alone is typically identified for use in inversions during 2D MASW processing, higher mode data can also provide useful information regarding the soil stratigraphy. In this study, not all models exhibited the presence of higher mode data. Therefore, an effort was made to consistently process the dispersion data in an attempt to recover a dispersive trend as close to the fundamental mode as possible. Although, in some cases, this required including dispersion data points along a trend of superposed higher modes. To illustrate this, Fig. 3e-f show the dispersion data from Fig. 3c-d after trimming and calculating statistics. Fig. 3e-f show the trimmed dispersion curve with the lower-bound trend that is presumably close to the fundamental mode, but should more accurately be termed a superposition of modes.

3.2. Calculating relative misfits

Once the dispersion curves were processed for all models, relative misfits between the control models (i.e., the half-space models) and their associated treatment models were calculated using the L1 norm of dispersion residuals. Although the L2 norm is more commonly used, various studies have found that using the L1 norm is equally applicable. Specifically, [25] found that using an L1 norm with FWI provides more accurate 2D V_s maps relative to the L2 norm, while [26] found that inverting electrical resistivity tomography data with L1 norm implementations allowed for better resolution when analyzing sharp boundaries between materials with high resistivity contrasts. Additionally, the L1 norm has an established low sensitivity to outliers when compared to the L2 norm. Therefore, the L1 norm misfit was deemed to be more suitable for this study. The equation is as follows:

$$\text{L1 misfit} = \sum_{i=1}^{n_f} \frac{|x_{ci} - x_{ti}|}{\sigma_{ci} n_f} \qquad (1)$$

where x_{ci} is the Rayleigh wave phase velocity of the control model at frequency f_i, x_{ti} is the Rayleigh wave phase velocity of a treatment model at f_i, σ_{ci} is the standard deviation of the control model's dispersion data at f_i, and n_f is the number of frequency samples being considered. From Eq. (1), it can be deduced that a misfit of one would correspond to a treatment dispersion curve that is on

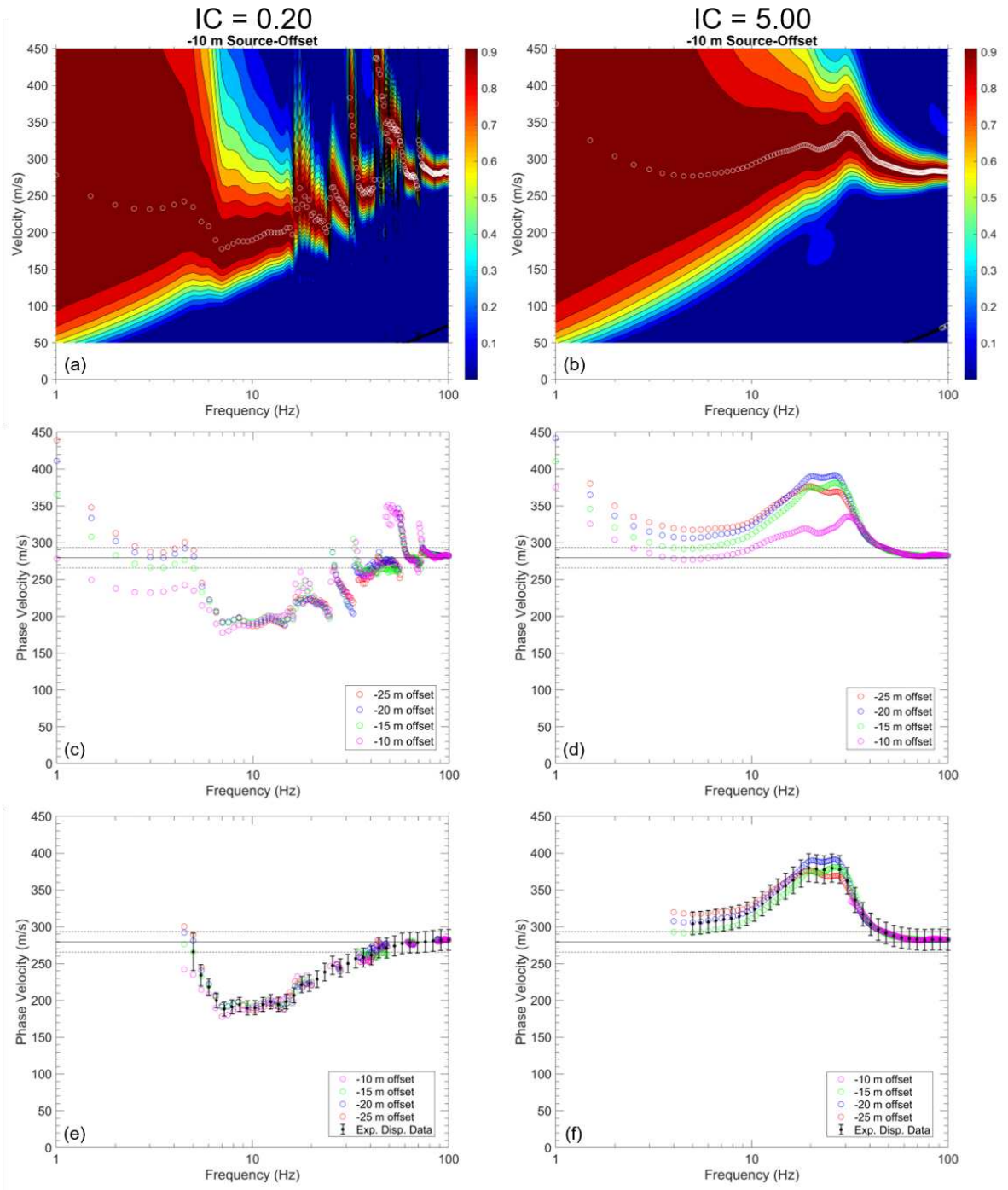

Figure 3. Dispersion data for two models containing an anomaly that is 2 m thick, 36 m wide, and at a top depth of 5 m. The shear-wave velocity of the surrounding soil is 300 m/s while the anomaly's shear-wave velocity is 60 m/s (left column) or 1,500 m/s (right column). Specifically, the model shown in the left column is model I0.20-H300-T2-D5-L36, while the right column is model I5.00-H300-T2-D5-L36. (a-b) show the corresponding dispersion images for the closest shot offset with peak energies identified as white hollow circles at each frequency. (c-d) show the raw dispersion data before trimming and calculating statistics. In both (c) and (d), the presence of higher modes is clearly visible. (e-f) show the same dispersion data from (c-d) after trimming and calculating statistics to obtain a lower-bound "fundamental mode" from the superposed higher modes. The solid black line in (c-f) represents the theoretical phase velocity of the half-space, while the dashed lines represent an assumed 5% coefficient of variation on phase velocity.

average one standard deviation away from the mean of a control dispersion curve. Therefore, a misfit less than one indicates a treatment model's dispersion curve is on average within the bounds of uncertainty of the control model's dispersion curve and not easily distinguishable from the control model. Note that a constant 5% COV was used to estimate the control models' dispersion uncertainty. Several blind studies have shown that experimental dispersion data can typically be resolved within 5% - 10% COV [27-28]. The lower COV value was chosen to again provide more favorable circumstances for detecting the anomalies in the models.

4. Results and discussion

Using Eq. (1), relative misfits were calculated between each treatment model and its corresponding control model. An example of a set of three treatment models compared to a control model is shown in Fig. 4. In this

case, the control model consists of a half-space with V_s equal to 150 m/s. Three different treatment models containing anomalies that are 1 m thick, 36 m wide, and with a V_s of 30 m/s were chosen. These models were selected so that a comparison between three different top depths could be made (specifically, models I0.20-H150-T1-D2-L36, I0.20-H150-T1-D6-L36, and I0.20-H150-T1-D14-L36 were chosen). For an anomaly placed at a depth of 2 m, 6 m, and 14 m, misfit values were measured as 4.4, 1.4, and 0.5, respectively. Fig. 4 visually demonstrates that increasing misfit values correspond directly to larger deviations between the control model and treatment models. A treatment model with a shallow anomaly and a misfit value of 4.4 is easily detectable; however, a treatment model with a deeper anomaly and a misfit of 0.5 is not easily detectable outside the bounds of typical dispersion data uncertainty. Additionally, these dispersion curves were plotted with respect to wavelength rather than frequency to better illustrate the effects the depth of the anomaly has on misfit values. The correspondence between wavelength and depth is apparent in Fig. 4 as the presence of a shallow anomaly (i.e., 2 m) causes the treatment model's dispersion curve to deviate from that of the control model at smaller wavelengths. However, for this same shallow anomaly the dispersion data begins to return to the half-space velocity at long wavelengths as they "see" through the anomaly and into the half-space beneath. Note that the misfit of each model is highly non-linear with depth. In particular, the difference in the misfit when the anomaly is at 2 m is significantly (by almost a factor of 3 times) larger than when it is at 6 m with the same being true for the 6 and 14 m depths. This non-linear relationship between depth and misfit (i.e., whether or not the anomaly is detectable) is discussed further when analyzing the trends in misfit values for all models.

After processing over 3,000 unique models, figures were created to summarize the trends observed in the misfit values (refer to Fig. 5-10). In these figures, the lateral dimension of each anomaly was normalized with respect to the length of the array used in the simulated tests. To summarize the results succinctly, plots were created for each unique combination of impedance contrast and half-space V_s as no acceptable form of velocity normalization could be found to combine all results. This was due in part to the observation that with all other parameters held constant (i.e., depth, thickness, and impedance contrast), absolute V_s of the half-space and anomaly are important and result in vastly different misfit values. These differences in misfit are believed to stem from non-equal wavelengths across models. Since wavelength is a function of velocity and frequency, it follows that higher velocities will result in larger wavelengths for similar frequencies and thus the potential to detect an anomaly with depth will vary depending on the velocities present at a site. To illustrate these differences, the overall maximum and minimum wavelengths (λ_{max} and λ_{min}, respectively) have been shown for each figure. Each figure was further separated by anomaly thickness and half-space (HS) velocity for ease of viewing. For plotting purposes, misfit values over 3.0 were all assigned the same color scale, as values of 3.0 and higher represent clearly detectable anomalies. Additionally, Table 3 has been provided, which summarizes the key findings of each set of figures.

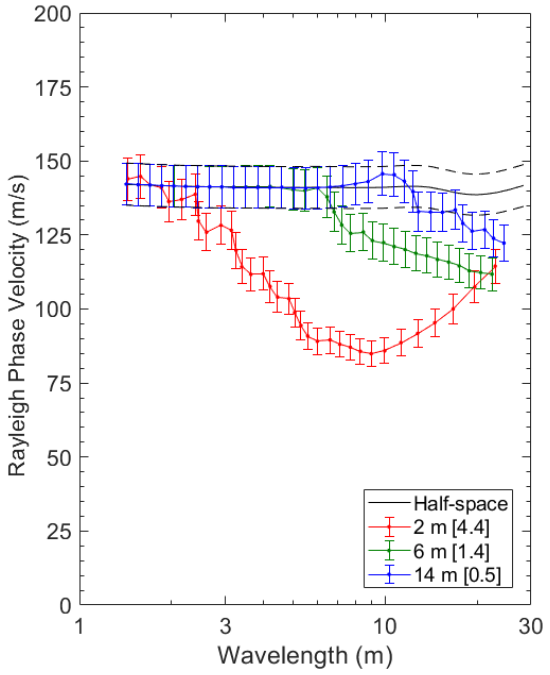

Figure 4. Comparison of dispersion data for models containing an anomaly that is 1 m thick and 36 m wide at varying top depths (2 m, 6 m, and 14 m). The shear wave velocity of the anomalies is 30 m/s while the surrounding soil has a shear wave velocity of 150 m/s. Note that as the top depth of the anomaly increases, the relative misfit values (indicated inside the legend in brackets []) for the respective dispersion curves decrease. The phase velocities are presented as a function of wavelength such that the trend regarding depth is more easily seen.

Each figure presents misfit values for a fixed impedance contrast as a function of the anomaly's top depth (vertical axis), normalized lateral extent (horizontal axis), HS velocity, and anomaly thickness. A clear boundary at a misfit value of 1.0 was included in order to indicate the zone above which an anomaly will most confidently be detected. Specifically, the colors above the boundary line (the gradient from green to red) indicate that an anomaly within this zone is likely to be detectable, while the colors below the boundary line (the gradient of blue colors) indicate anomalies within this zone will be more difficult to detect. This is not to say that the blue zone represents that an anomaly is impossible to detect; rather, the blue zone represents that an anomaly cannot be detected with a high degree of confidence.

Fig. 5 shows the results for an impedance contrast of 0.67. Fig. 5a-c are for models generated with a half-space V_s of 150 m/s while Fig. 5d-f are for a half-space V_s of 300 m/s. Both rows are listed in order of increasing anomaly thickness, such that Fig. 5a-c and Fig. 5d-f are for anomalies that are 1, 2, and 4 m thick, respectively. From these figures, as expected, it is clear that an increase in anomaly thickness directly corresponds to an increase in the chance to detect it. The same is true with increasing lateral extent of the anomaly relative to the length of the array. However, despite the expected trends showing an increase in detectability for larger anomalies, the results for this impedance contrast indicate it may be more difficult than anticipated to easily detect anomalies. For example, a 1 m-thick anomaly must be longer than at least three-quarters of the array length to have a high chance of being detected, while a 4 m-thick anomaly must be

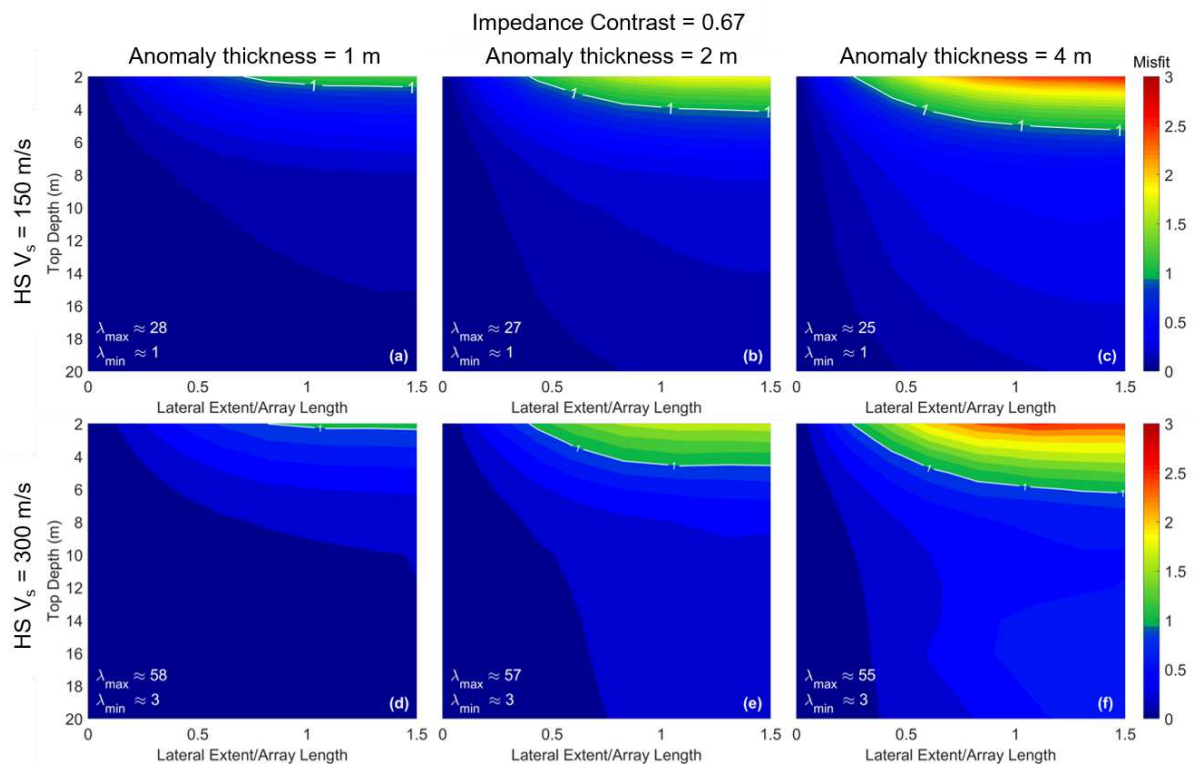

Figure 5. Summary plots of misfit values for an impedance contrast of 0.67. While all figures represent the same impedance contrast, (a-c) are for models containing a half-space with V_s equal to 150 m/s while (d-f) are for a half-space V_s of 300 m/s. Each row is listed in order of increasing anomaly thickness, such that (a-c) and (d-f) are for anomalies that are 1 m, 2 m, and 4 m thick, respectively. From these figures, it can be deduced that as an anomaly increases in thickness, the likelihood of detecting it increases (as indicated by higher misfit values with warmer colors). Additionally, the maximum depth at which an anomaly may be detected increases as the thickness increases. For higher half-space V_s values (d-f), longer wavelengths may be measured relative to lower V_s values (a-c), resulting in a higher chance of detecting anomalies at depth.

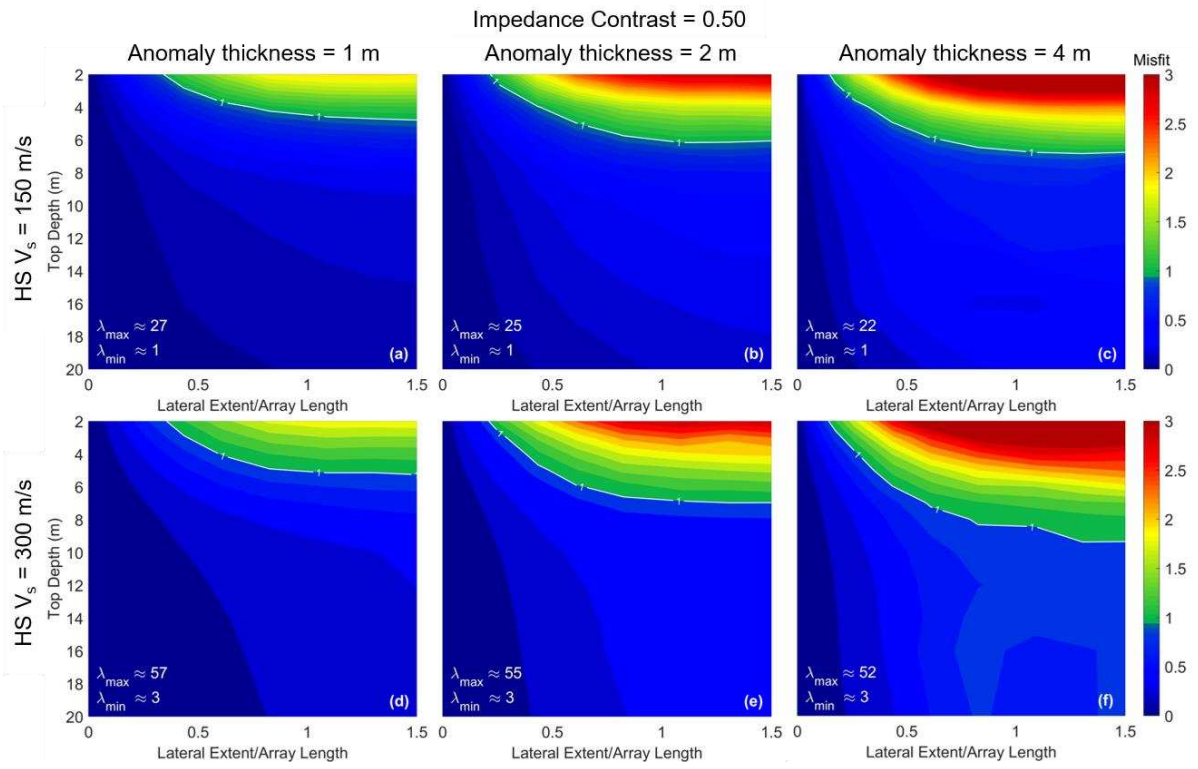

Figure 6. Summary plots of misfit values for an impedance contrast of 0.50. While all figures represent the same impedance contrast, (a-c) are for models containing a half-space with V_s equal to 150 m/s while (d-f) are for a half-space V_s of 300 m/s. Each row is listed in order of increasing anomaly thickness, such that (a-c) and (d-f) are for anomalies that are 1 m, 2 m, and 4 m thick, respectively. These figures show a marked difference from Fig. 5 in that across all models, anomalies in general are more likely to be detected given a higher impedance contrast between an anomaly and surrounding soil. In particular, the top depth at which a 1 m-thick anomaly may be detected has nearly doubled, and the likelihood of detecting 2 m- and 4 m-thick anomalies has significantly increased for similar depths.

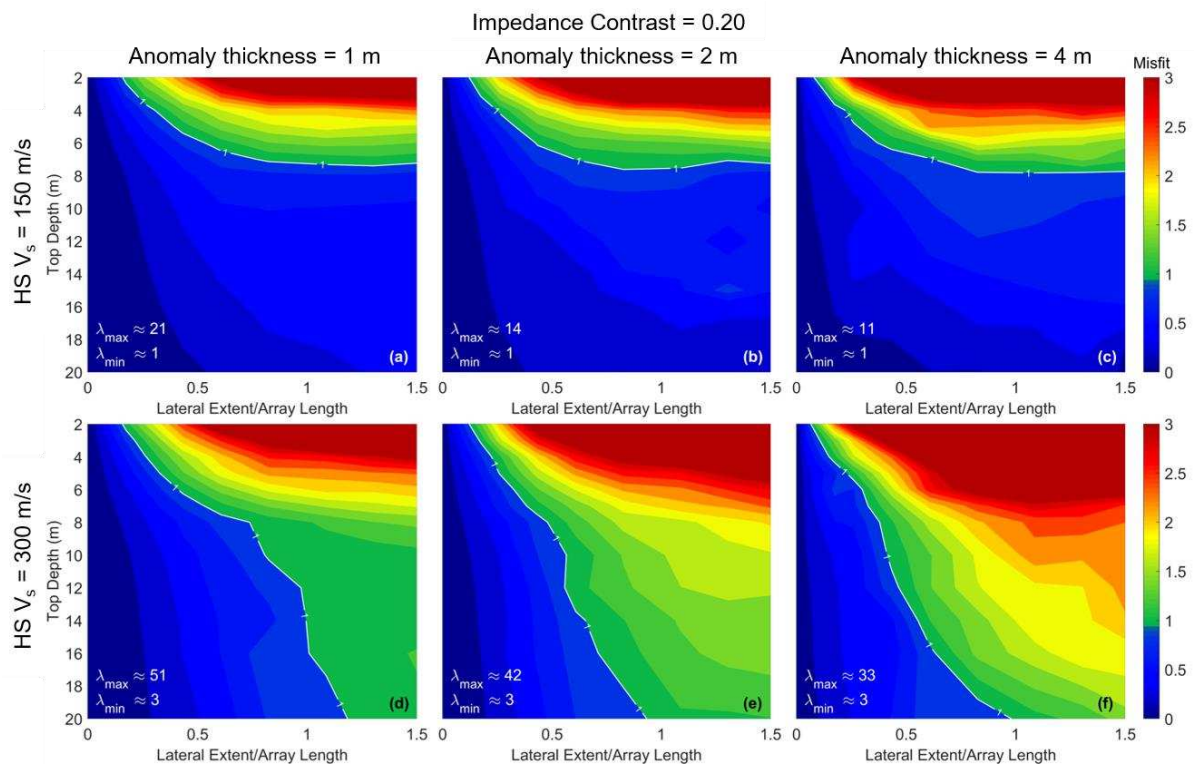

Figure 7. Summary plots of misfit values for an impedance contrast of 0.20. While all figures represent the same impedance contrast, (a-c) are for models containing a half-space with V_s equal to 150 m/s while (d-f) are for a half-space V_s of 300 m/s. Each row is listed in order of increasing anomaly thickness, such that (a-c) and (d-f) are for anomalies that are 1 m, 2 m, and 4 m thick, respectively. Note that these figures vary significantly compared to Fig. 5 and Fig 6. Specifically, (d-f) show that for an anomaly that is roughly the same length or longer than an array, the likelihood of detecting it is still possible even at relatively large depths. This is likely due to the high impedance contrast providing data for treatment models that are easily distinguishable from that of the control models as many dispersion curves exhibited higher modes.

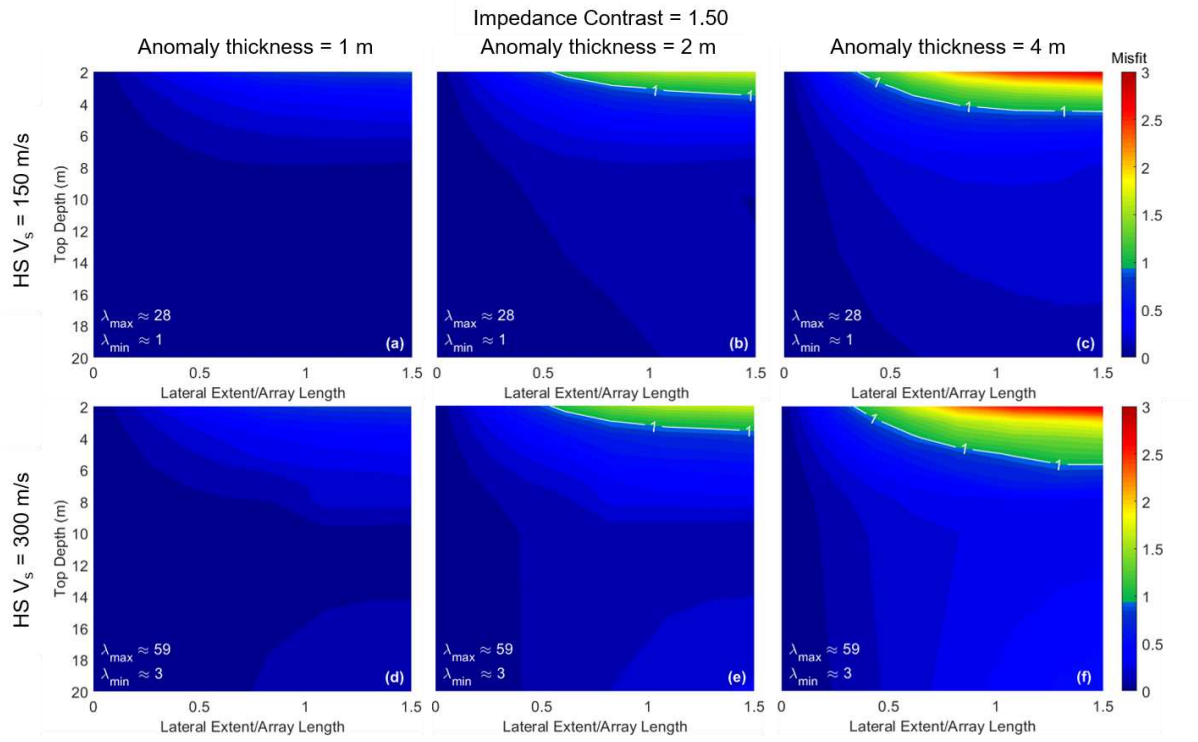

Figure 8. Summary plots of misfit values for an impedance contrast of 1.5. While all figures represent the same impedance contrast, (a-c) are for models containing a half-space with V_s equal to 150 m/s while (d-f) are for a half-space V_s of 300 m/s. Each row is listed in order of increasing anomaly thickness, such that (a-c) and (d-f) are for anomalies that are 1 m, 2 m, and 4 m thick, respectively. These models are similar to those presented in Fig. 5; however, these models contain anomalies that are stiffer than the surrounding material. Although it is difficult to detect 1 m-thick anomalies, the possibility of detection increases as the thickness of the anomaly increases, similar to previously discussed trends. Additionally, when compared to Fig. 5, stiffer anomalies are shown to be more difficult to detect than softer anomalies.

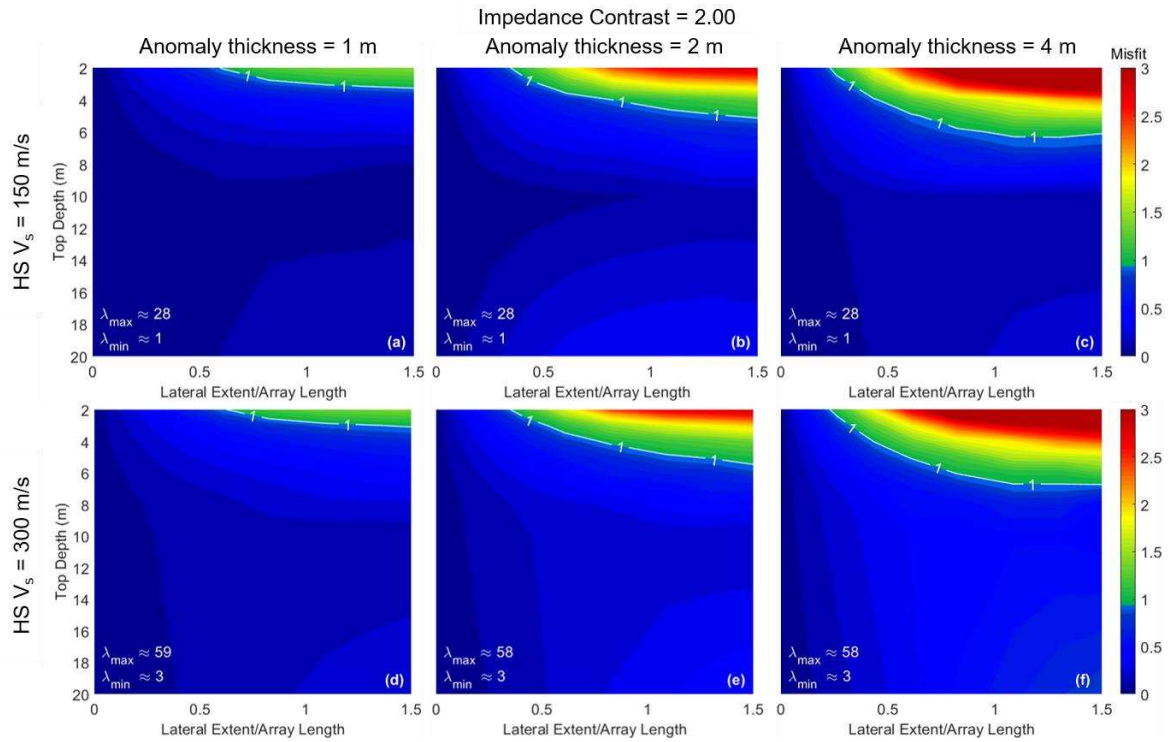

Figure 9. Summary plots of misfit values for an impedance contrast of 2.0. While all figures represent the same impedance contrast, (a-c) are for models containing a half-space with V_s equal to 150 m/s while (d-f) are for a half-space V_s of 300 m/s. Each row is listed in order of increasing anomaly thickness, such that (a-c) and (d-f) are for anomalies that are 1 m, 2 m, and 4 m thick, respectively. Additionally, these models contain anomalies that are stiffer than the surrounding material. Compared to an impedance contrast of 1.5, these plots show that a larger impedance contrast results in higher detection of anomalies. As thickness increases, the lower bound of detectability also increases, similar to Fig. 6.

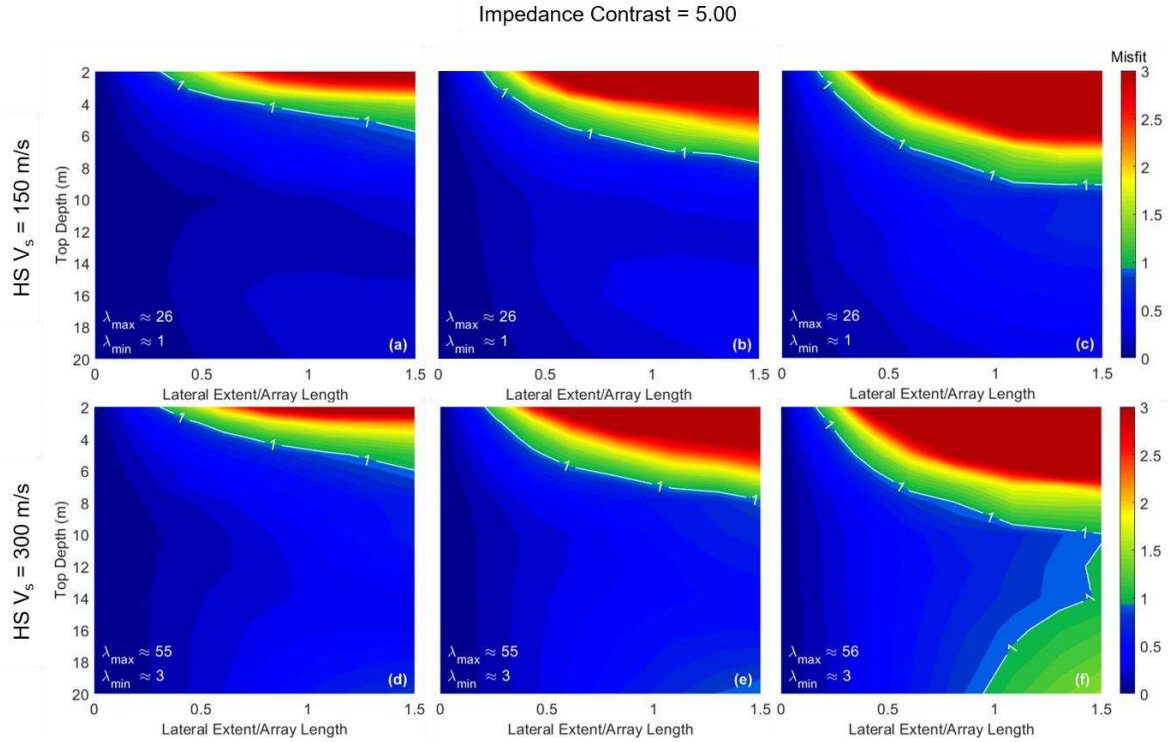

Figure 10. Summary plots of misfit values for an impedance contrast of 5.0. While all figures represent the same impedance contrast, (a-c) are for models containing a half-space with V_s equal to 150 m/s while (d-f) are for a half-space V_s of 300 m/s. Each row is listed in order of increasing anomaly thickness, such that (a-c) and (d-f) are for anomalies that are 1 m, 2 m, and 4 m thick, respectively. Additionally, these models contain an anomaly that is stiffer than the surrounding material. It should be noted that these models provided erratic data at higher depths. Particularly, models containing a 4 m-thick anomaly in soil with a V_s of 300 m/s exhibited dispersion data that cannot "see" through an anomaly, which resulted in higher misfits than otherwise expected. Therefore, results below roughly 10 to 12 m are not considered to be trustworthy.

Table 3. Summary of results for all models

Imp. Contrast	Half-space V_s (m/s)	Anomaly Thickness (m)	Max. Likely Detectable Depth (m)	Min. Likely Detectable Size Relative to Array	Min. Likely Detectable Lateral Extent (m)
0.67	150	1	3	0.70	16
		2	4	0.40	9
		4	5.5	0.25	6
	300	1	2.5	0.80	18
		2	4.5	0.40	9
		4	6	0.25	6
0.50	150	1	5	0.35	8
		2	6	0.23	5
		4	7	0.15	3.5
	300	1	5.5	0.35	8
		2	7	0.21	5
		4	9.5	0.15	3.5
0.20	150	1	7[1]	0.15	3.5
		2	7[1]	0.13	3
		4	7.5[1]	0.08	2
	300	1	+20[2]	0.15	3.5
		2	+20[2]	0.12	3
		4	+20[2]	0.08	2
1.5	150	1	-	-	-
		2	3.5	0.55	12.5
		4	4.5	0.35	8
	300	1	-	-	-
		2	3.5	0.55	12.5
		4	6	0.35	8
2.0	150	1	3	0.60	14
		2	5	0.35	8
		4	6	0.25	6
	300	1	3	0.63	14.5
		2	5.5	0.35	8
		4	7	0.23	5
5.0	150	1	5.5	0.30	7
		2	7.5	0.20	4.5
		4	9	0.18	4
	300	1	6	0.30	7
		2	8	0.20	4.5
		4	10[3]	0.15	3.5

1. Although it was expected that increases in thickness would result in increases in maximum detectable depth, these data showed unusual trends. Specifically, measured wavelengths were shown to decrease with changes in thickness, as further described in Sec. 4.
2. The depths of detection for these models extended beyond the maximum depth of 20 m used in this study. This was due to the presence of significant higher modes, which resulted in large misfit values for each set of models that resulted in no visible lower bound for a misfit of 1.0.
3. It was expected that a 4 m-thick anomaly would show an increase in maximum detectable depth for this impedance contrast and half-space V_s pairing. However, the dispersion trends showed that as the depth to the anomaly increased, the chance to "see" through the anomaly decreased, which led to increases in misfit as further described in Sec. 4.

longer than at least a quarter of the array length. Further, 1 m-thick anomalies can only be confidently detected up to 3 m deep, while 4 m-thick anomalies can only be confidently detected up to about 6 m deep. When comparing the change in half-space V_s between respective sets of models, it is shown that an increase in half-space V_s also corresponds to an increase in general detectability. This is believed to be related to the increase in the overall maximum wavelength present for each set of models. As previously mentioned, higher velocities will result in longer wavelengths for a given frequency, which is shown in Fig. 5d-f where the maximum wavelength present for each set of models is nearly double the maximum wavelength for the corresponding sets in Fig. 5a-c. Due to this, it is understandable that an increase in overall velocity at a given impedance contrast results in an increase in the possibility of deeper anomaly detection. These results are further tabulated in Table 3, such that trends in the maximum likely detectable depth as well as the minimum likely detectable size of an anomaly may be more easily visualized. It should be noted that the results listed in Table 3 are approximate values and represent the boundaries of likely detection.

Fig. 6 presents similar misfit summary plots for models with an impedance contrast of 0.50. These results show that for a larger impedance contrast, the ability to detect anomalies increases. In particular, the depth at which a 1 m-thick anomaly can be detected has nearly doubled, which can be seen when comparing Fig. 5a and Fig 5d with Fig. 6a and Fig. 6d, respectively. Additionally, the size of a detectable anomaly is smaller. Like Fig. 5, the maximum wavelengths present in the high velocity models (Fig. 6d-f) are more than double the wavelengths present in similar sets of models with lower velocities (Fig. 6a-c), and as such, the maximum depth at which anomalies can be confidently detected is greater when higher velocities are present. This trend further supports the assertion that the wavelengths present for each set of models are directly related to the chance of detecting anomalies at increasing depths.

Fig. 7 presents the misfit values for an impedance contrast of 0.20. These figures are notably distinct from those shown previously in that Fig. 7a-c show almost no change in the maximum depth at which an anomaly can be reasonably detected despite increases in thickness. Likewise, Fig. 7d-f show that increases in anomaly thickness do not show visible effects on the maximum depth of detectability, although this is at least partially due to the misfit boundary of 1.0 extending beyond the depths used in this study. Regarding Fig. 7d-f, the absence of a maximum depth of detection is likely due to the data provided by high impedance contrasts. Although the maximum wavelengths measured for each set of models reveal that it is possible to detect anomalies at relatively large depths, the dispersion data obtained for each of these models was quite complicated with significant higher modes. This meant that, despite using a lower-bound dispersion trend from superposed modes, the dispersion curves for various treatment models were still significantly distinguishable from that of the control model. Therefore, it was found that for models containing higher velocities and an impedance contrast as significant as 0.20, the chance of detecting anomalies in general is more probable than compared to models containing lower velocities. Based on Fig. 7d-f, it was assumed that Fig. 7a-c would also show an increase in misfit as thickness increases. However, the maximum depth for the misfit boundary of 1.0 is shown to remain relatively constant for each thickness. This is likely due to the maximum wavelengths shown in Fig. 7b and Fig. 7c as they reveal that the depth of detection should be roughly 7 and 6 m, respectively, if using an estimate of $\lambda/2$. Therefore, for these two sets of models, it is reasonable that the maximum depth of detection does not significantly increase with changes to anomaly thickness as the anomaly, regardless of its thickness, is already nearly undetectable at this depth.

Fig. 8-10 present the misfit values for models containing an anomaly that is stiffer than the surrounding half-space. When comparing each set of models, it is clear that overall, it is more difficult to detect a stiff inclusion as opposed to a soft one. In particular, Fig. 8 shows that it is difficult to detect a 1 m-thick anomaly regardless of the half-space V_s. Both the 2 m- and 4 m-thick anomalies are shown to be detectable, but when compared to Fig. 5b-c, the boundary at which a misfit of 1.0 is present is shallower for models containing a stiff anomaly. In terms of an anomaly's lateral extent, the minimum size required for an anomaly to be detectable does not significantly change depending on whether the anomaly is soft or stiff relative to the surrounding soil (compare for example Fig. 5 and Fig. 8). Fig. 9 presents misfit values for models with an impedance contrast of 2.0, again illustrating that stiff anomalies are overall more difficult to detect than soft anomalies when compared with Fig. 6.

When examining Fig. 10, which represents models with an impedance contrast of 5.0, it is clear that the results for models generated with a half-space V_s of 300 m/s differ significantly at deeper depths compared to those generated with a V_s of 150 m/s. In particular, models containing a 4 m-thick anomaly (Fig. 10f) show that the potential to detect an anomaly actually increases for depths below 16 m. This unexpected change in misfit can be explained with careful consideration of the dispersion data. For an anomaly placed at various depths, with all other variables held constant, there are four stages of note. First, the anomaly is near the surface and can easily be detected (i.e., has a high misfit). Second, the anomaly moves deeper and although it is still being "seen" by the surface wave, its velocity is being averaged with the material above and below it and is therefore less easily detected (i.e., has a relatively lower misfit). Third, the anomaly approaches the bottom-most range that the surface wave can "see", and since it is in effect no longer being averaged with a material of a different velocity below it, the anomaly appears to be easier to detect (i.e., misfit begins to increase). Fourth, the top of the anomaly is below the maximum detectable depth and therefore cannot be detected (i.e., misfit is approximately 0). This trend is illustrated in Fig. 11 using anomalies represented in Fig. 10f for a lateral extent of 36 m with increasing top depths of 2, 14, and 20 m. Specifically, the first three stages are shown. When the depth of the anomaly increases from 2 to 14 m, the misfit value is shown to decrease significantly from 12.6 to 1.0. However, when the depth of the anomaly increases to 20 m, the misfit slightly

increases to 1.6. The fourth stage in which the anomaly is no longer detected, i.e., when the misfit approaches zero, is not shown as this stage extended beyond the depths used in this study. For each of the conditions considered, all four stages may or may not be clearly present, although this lends a physical explanation of the data in regard to the contour plots presented herein.

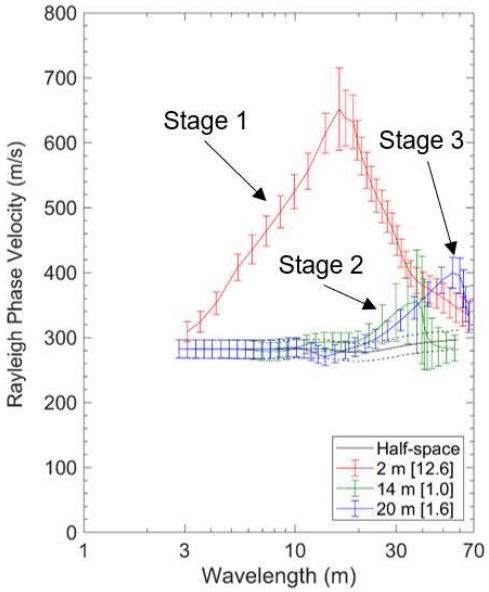

Figure 11. Three stages of detectability are shown for an anomaly that is 4 m-thick, 36 m wide, and with increasing top depths of 2, 14, and 20 m, which are indicative of the trends shown in Fig. 10f. Stage 1 shows that the anomaly is easily detectable, as indicated by the high misfit of 12.6. As the anomaly is placed deeper (stage 2), its velocity begins to be averaged with the surrounding soil, leading to a lower misfit of 1.0. Once the anomaly is placed at relatively larger depths (stage 3), surfaces waves can no longer "see" through the anomaly and the dispersion data do not return to the theoretical half-space velocity as expected, which leads to higher misfits. Stage 4, in which this anomaly should no longer be detectable, is not shown as this stage occurs beyond 20 m, which was the maximum depth used in this study.

5. Conclusion

To address the limited literature available regarding the quantitative ability of the MASW method to detect subsurface anomalies, typical testing procedures were simulated using synthetic control (i.e., without an anomaly) and treatment (i.e., with an anomaly) models. The misfit between the dispersion data of the control and treatment models were summarized quantitatively and used to illustrate whether a particular anomaly could or could not likely be detected. To allow for practical usage of this study, the quantitative misfit values were used to create example feasibility plots such that the likelihood of detecting an anomaly of a given geometry can be assessed prior to performing the field acquisition.

In short, the results presented in Fig. 5-10 and Table 3 reveal that the ability to detect an anomaly is largely dependent on its impedance contrast with the surrounding material and to a lesser extent on its size. In particular, lower impedance contrasts (soft anomalies) allow for greater chances of detection when compared to higher impedance contrasts (stiffer anomalies). Furthermore, a site with higher velocities leads to greater chances for detection of anomalies at depth compared to a site containing soils with low velocities due to an increase in the measured wavelengths, provided the frequency range measured at both sites is consistent. At impedance contrasts greater than 1.0, an anomaly must be roughly half the length of the array used during testing to likely be detected, whereas at an impedance contrast less than 1.0, the anomaly may be as small as a quarter of the array length. As expected, the results show that as the thickness of an anomaly increases, the potential to detect it increases, while an increase in depth to the top of the same anomaly results in a decrease in its detectability. It should be noted again that while a misfit of 1.0 was used as a general guideline for the boundary of easy/likely detection in this study, misfits below 1.0 do not strictly indicate that an anomaly will not be detected; rather, the authors have interpreted a misfit below 1.0 to indicate that these anomalies will be more difficult, or in general less likely, to be detected given typical levels of experimental dispersion data uncertainty.

Although this study emphasized the importance of detecting anomalies when performing site characterization, the ability to accurately resolve irregular velocity profiles through inversion is similarly significant. The authors acknowledge that detecting an anomaly is present does not necessarily mean that the anomaly may be resolved in terms of its shape and velocity. Although we hope this work may be useful to others planning site characterization studies using 2D MASW for anomaly detection, further work is needed to determine the potential for resolving an anomaly's shape, stiffness, and location given that it can likely be detected based on its dispersion signature.

Acknowledgement

This material is based upon work supported by the National Science Foundation Graduate Research Fellowship Program under Grant No. DGE – 1610403. Any opinions, findings, and conclusions or recommendations expressed in this material are those of the authors and do not necessarily reflect the views of the National Science Foundation.

Additionally, the authors would like to thank the Texas Advanced Computing Center (TACC) for providing access to the high-performance computing resource Stampede2, which was invaluable for completing this study. The authors would also like to express gratitude towards the creators of DENISE for releasing their code as an open-source project, which proved to be the foundation for this study.

References

[1] Hirsch, M., Bentley, L. R., and Dietrich, P. "A comparison of electrical resistivity, ground penetrating radar and seismic refraction results at a river terrace site", Journal of Environmental & Engineering Geophysics, 13(4), pp. 325–333, 2008. https://doi.org/10.2113/JEEG13.4.325.

[2] Mirzanejad, M., Tran, K. T. "3D viscoelastic full waveform inversion of seismic waves for geotechnical site investigation", Soil Dynamics and Earthquake Engineering, 122, pp. 67-78, 2019. https://doi.org/10.1016/j.soildyn.2019.04.005

[3] Rahimi, S., Wood, C. M., Coker, F., Moody, T., Bernhardt-Barry, M., Kouchaki, B. M. "The combined use of MASW and resistivity surveys for levee assessment: A cast study of the Melvin Price Reach of the Wood River Levee", Engineering Geology, 241, pp. 11-24, 2018. https://doi.org/10.1016/j.enggeo.2018.05.009

[4] Xia, J., Chen, C., Li, P. H., Lewis, M. J. “Delineation of a collapse feature in a noisy environment using a multichannel surface wave technique”, Geotechnique, 54(1), pp. 17-27, 2004. https://doi.org/10.1680/geot.2004.54.1.17

[5] Park, C. B., Miller, R. D., Xia, J. “Multichannel analysis of surface waves”, Geophysics, 64(3), pp. 800-808, 1999. https://doi.org/10.1190/1.1444590

[6] Nolet, G., Panza, G. F. “Array analysis of seismic surface waves: Limits and possibilities”, Pure and Applied Geophysics, 114(5), pp. 775–790, 1976. https://doi.org/10.1007/BF00875787

[7] Zywicki, D. J. “Advanced Signal Processing Methods Applied to Engineering Analysis of Seismic Surface Waves”, Georgia Institute of Technology, 1999.

[8] Xia, J., Miller, R. D., Park, C. B., Hunter, J.A., Harris, J.B. “Comparing shear-wave velocity profiles from MASW with borehole measurements in unconsolidated sediments, Fraser River Delta, B.C., Canada”, Journal of Environmental and Engineering Geophysics, 5(3), pp. 848-870, 2000. https://doi.org/10.4133/JEEG5.3.1

[9] Groves, P., Cascante, G., Dundas, D., Chatterji, P. K. “Use of geophysical methods for soil profile evaluation”, Canadian Geotechnical Journal, 48(9), pp. 1364-1377, 2011. https://doi.org/10.1139/t11-044

[10] Ismail, A., Denny, F. B., Metwaly, M. “Comparing continuous profiles from MASW and shear-wave reflection seismic methods”, Journal of Applied Geophysics, 105, pp. 67-77, 2014. https://doi.org/10.1016/j.jappgeo.2014.03.007

[11] Mahvelati, S., Coe, J.T. “The use of two dimensional (2D) multichannel analysis of surface waves (MASW) testing to evaluate the geometry of an unknown bridge foundation”, In: Geotechnical Frontiers, Orlando, FL, United States, 2017, pp. 657-666. https://doi.org/10.1061/97807844804441.069

[12] Nolan, J. J., Sloan, S. D., Broadfoot, S.W., McKenna, J. R., Metheny, O. M. "Near-surface void identification using MASW and refraction tomography techniques", SEG Technical Program Expanded Abstracts, pp. 1401-1405, 2011. https://doi.org/10.1190/1.3627464

[13] Pan, Y., Gao, L., Bohlen, T. “High-resolution characterization of near-surface structures by surface-wave inversions: from dispersion curve to full waveform”, Surveys in Geophysics, 40(2), pp. 167-195, 2019. https://doi.org/10.1007/s10712-019-09508-0

[14] Köhn, D., De Nil, D., Kurzmann, A., Przebindowska, A., Bohlen, T. “On the influence of model parametrization in elastic full waveform tomography”, Geophysical Journal International, 191(1), pp. 325-345, 2012. https://doi.org/10.1111/j.1365-246X.2012.05633.x

[15] Stokoe, K. H., Cox, B. R., Lin, Y. C., Jung, M. J., Menq, F. Y., Bay, J. A., ... Wong, I. “Use of intermediate to large vibrators as surface wave sources to evaluate Vs profiles for earthquake studies”, In: 19th EEGS Symposium on the Application of Geophysics to Engineering and Environmental Problems, Seattle, WA, United States, 2006, pp. 1241-1258. https://doi.org/10.4133/1.2923582

[16] Park, C. B. "MASW – Horizontal resolution in 2D Shear-velocity (Vs) Mapping", Kansas Geological Survey, Lawrence, KS, United States, KGS Open-file Report, 2005.

[17] Foti, S., Hollender, F., Garofalo, F., et al. “Guidelines for the good practice of surface wave analysis: a product of the InterPACIFIC project”, Bulletin of Earthquake Engineering, 16(6), pp. 2367-2420, 2018. https://doi.org/10.1007/s10518-017-0206-7

[18] Mohamed, A. M. E., Abu El Ata, A. S. A., Abdel Azim, F., Taha, M. A. “Site-specific shear wave velocity investigation for geotechnical engineering applications using seismic refraction and 2D multi-channel analysis of surface waves”, NRIAG Journal of Astronomy and Geophysics, 2(1), pp. 88-101, 2013. https://doi.org/10.1016/j.nrjag.2013.06.012

[19] Suto, K., Kristinof, R. “An MASW survey to assess flood damaged road – A case history”, In: Symposium on the Application of Geophysics to Engineering and Environmental Problems, Boston, MA, United States, 2014. https://doi.org/10.4133/SAGEEP.27-143

[20] Ivanov, J. M., Johnson, C. D., Lane Jr., J. W., Miller R. D., Clemens, D. “Near-surface evaluation of Ball Mountain Dam, Vermont, using multi-channel analysis of surface waves (MASW) and refraction tomography seismic methods on land-streamer data, SEG Technical Program Extended Abstracts, pp. 1454-1458, 2009. https://doi.org/10.1190/1.3255123

[21] Debeglia, N., Bitri, A., Thierry, P. “Karst investigations using microgravity and MASW; Application to Orleans, France”, Near Surface Geophysics, 4(4), pp. 215-225, 2006. https://doi.org/10.3997/1873-0604.2005046

[22] Shakir, A. M., Foti, S., Garofalo, F., Hijab, B. R., Laftah, A. A. “Laterally constrained inversion of surface wave data at Najaf city (Iraq)”, Soil Dynamics and Earthquake Engineering, 45, pp. 89-95, 2013. https://doi.org/10.1016/j.soildyn.2012.11.003

[23] Ivanov, J., Miller, R. D., Lacombe, P., Johnson, C. D., Lane Jr., J. W. “Delineating a shallow fault zone and dipping bedrock strata using multichannel analysis of surface waves with a land streamer”, Geophysics, 71(5), pp. A39-A42, 2006. https://doi.org/10.1190/1.2227521

[24] Cox, B. R., Wood, C. M. “Surface wave benchmarking exercise: Methodologies, results, and uncertainties”, In: GeoRisk 2011, Atlanta, GA, United States, 2011, pp. 845–852. https://doi.org/10.1061/41183(418)89

[25] Brossier, R., Operto, S., Virieux, J. “Which data residual norm for robust elastic frequency-domain full waveform inversion?”, Geophysics, 75(3), pp. R37-R46, 2010. https://doi.org/10.1190/1.3379323

[26] Chambers, J. E., Kuras, O., Meldrum, P. I., Ogilvy, R. D., Hollands, J. “Electrical resistivity tomography applied to geologic, hydrogeologic, and engineering investigations at a former waste-disposal site”, Geophysics, 71(6), pp. B231-B239, 2006. https://doi.org/10.1190/1.2360184

[27] Cox, B.R., Wood, C.M., Teague, D.P. “Synthesis of the UTexas1 Surface Wave Dataset Blind-Analysis Study: Inter-Analyst Dispersion and Shear Wave Velocity Uncertainty”, In: ASCE GeoCongress 2014: Geo-Characterization and Modeling for Sustainability, Atlanta, GA, United States, 2014, pp. 23-26. https://doi.org/10.1061/9780784413272.083

[28] Garofalo, F., Foti, S., Hollender, F., Bard, P.-Y., Cornou, C., Cox, B.R., Ohrnberger, M., Sicilia, D., Asten, M., Di Giulio, G., Forbriger, T., Guiller, B., Hayashi, K., Martin, A., Matsushima, S., Mercerat, D., Poggi, V., Yamanaka, H. “InterPACIFIC Project: Comparison of Invasive and Non-Invasive Methods for Seismic Site Characterization Part I: Intra-Comparison of Surface Wave Methods”, Soil Dynamics and Earthquake Engineering, 82(1), pp. 222-240, 2016. https://doi.org/10.1016/j.soildyn.2015.12.010